Chemical Science

ROYAL SOCIETY OF CHEMISTRY

EDGE ARTICLE

View Article Online
View Journal | View Issue

Cite this: *Chem. Sci.*, 2022, **13**, 996

All publication charges for this article have been paid for by the Royal Society of Chemistry

An asymmetric 2,3-fluoranthene imide building block for regioregular semiconductors with aggregation-induced emission properties†

Xianglang Sun,[a] Ming-Yun Liao,[b] Xinyu Yu,[a] Ying-Sheng Wu,[b] Cheng Zhong,[c] Chu-Chen Chueh,[b] Zhen Li[c] and Zhong'an Li*[a]

For organic semiconductors, the development of electron-deficient building blocks has lagged far behind that of the electron-rich ones. Moreover, it remains a significant challenge to design organic molecules with efficient charge transport and strong solid-state emission simultaneously. Herein, we describe a facile synthetic route toward a new π-acceptor imide building block, namely 2,3-fluoranthene imide, based on which four regioregular small molecules (**F1**–**F4**) are synthesized by tuning the imide orientations and the central linkage bridges. All molecules exhibit attractive aggregation-induced emission (AIE) characteristics with strong far-red emission in the powder state, and **F3** shows the highest photoluminescence quantum yield of 5.9%. **F1** and **F3** with a thiophene bridge present an obvious p-type characteristic, while for **F3** with an outward imide orientation, the maximum hole mobility from a solution-processed field-effect transistor (FET) device reaches 0.026 $cm^2 V^{-1} s^{-1}$, being ~10^4 times higher than the value of **F1** with an inward imide orientation. By using a fluorinated thiophene bridge, the resulting **F2** and **F4** can be turned into n-type semiconductors, showing an electron mobility of ~1.43×10^{-4} and ~3.34×10^{-5} $cm^2 V^{-1} s^{-1}$, respectively. Our work not only demonstrates that asymmetric 2,3-fluoranthene imide is a promising building block for constructing organic materials with high carrier mobility and strong solid-state emission, but also highlights the importance of regioregular structures in the materials' properties.

Received 6th December 2021
Accepted 10th December 2021

DOI: 10.1039/d1sc06807e

rsc.li/chemical-science

Introduction

Organic semiconductors show great importance for next-generation flexible and printed optoelectronic devices as well as biomedicines.[1–4] Among them, donor–acceptor (D–A) type π-conjugated systems have received the most interest because their optical and electronic properties can be conveniently and precisely adjusted by changing the D and A units.[5–10] However, compared to the diverse D units, the development of A units is severely restricted by the synthetic challenges of reduced reactivity caused by the electron-withdrawing groups.[11–14] Currently, arene imides such as perylene diimide (PDI) and naphthalene diimide (NDI) (Fig. 1a) are two of the most successful A units for organic optoelectronics due to their straightforward synthesis, deep lowest unoccupied molecular orbital (LUMO) level, facile material accessibility, *etc.*[15–21] However, due to the strong π–π intermolecular interactions as a result of highly planar π-conjugated structures, they usually suffer from aggregation-caused quenching (ACQ) in the solid state that limits their further applications.[22–25] Thus, it remains a challenge to design organic semiconductors with both high carrier mobility and strong solid-state emission, which thus warrants the exploration of new elementary building blocks.[26–31]

Fluoranthene is one typical polycyclic aromatic hydrocarbon, which possesses a rigid, planarized structure that is beneficial for intramolecular charge transport *via* π–π stacking. Moreover,

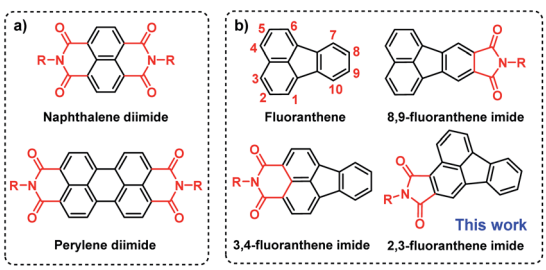

Fig. 1 Structures of (a) perylene diimide (PDI) and naphthalene diimide (NDI) and (b) fluoranthene and fluoranthene-fused imide derivatives.

[a]*Key Laboratory for Material Chemistry of Energy Conversion and Storage, Ministry of Education, School of Chemistry and Chemical Engineering, Huazhong University of Science and Technology, Wuhan, 430074, China. E-mail: lizha@hust.edu.cn*

[b]*Department of Chemical Engineering, National Taiwan University, Taipei, 10617, Taiwan*

[c]*Sauvage Center for Molecular Sciences, Department of Chemistry, Wuhan University, Wuhan, 430072, China*

† Electronic supplementary information (ESI) available. See DOI: 10.1039/d1sc06807e

it can be regarded as a basic unit of fullerene, exhibiting electron-deficient characteristics due to the central five-membered ring.[32–34] In this regard, the electron-deficient fluoranthene should be a suitable building block for imide-based semiconductors. Indeed, fluoranthene-fused imides have been successfully developed as non-fullerene acceptors for organic solar cells, the power conversion efficiency (PCE) of which can reach up to 3.12%.[35–39] Nonetheless, the structural diversity and synthetic strategy of fluoranthene imides are still limited (Scheme S1†). At present, the imidization sites of fluoranthene are mainly restricted to the 3, 4-sites or 8, 9-sites (Fig. 1b), as limited by the synthetic challenges of functionalization at other sites.[38,40–42] Besides, the applicability of fluoranthene derivatives including fluoranthene imides in organic field-effect transistors (OFETs) has rarely been explored so far.[43,44]

Recently, our group developed a facile synthetic route to functionalize fluoranthene at the 2,3-sites for the first time, that is, using dibenzofulvene as the diene to undergo a typical Diels–Alder reaction, rather than using acenaphthenequinone in most cases.[45] The resulting 2,3-dicyanofluoranthene unit was shown as an efficient electron-deficient core to construct D–A type dopant-free hole transporting materials for perovskite solar cells.[45,46] Therefore, it would be interesting to know whether this is also a feasible synthetic method to develop new fluoranthene imide building blocks. Herein, we successfully synthesize 2,3-fluoranthene imide through a simple one-pot reaction (Fig. 1). We find that the 4-site of 2,3-fluoranthene imide exhibits an enhanced reactivity compared to the 9-site, thus allowing us to synthesize two types of regioregular small molecules with different imide orientations (**F1–F4**, Fig. 2a). By regulating the imide orientation and the central linkage bridge, we show that the molecular configuration and packing of the derived molecules can be accordingly adjusted to not only realize high hole mobility and attractive aggregation-induced emission (AIE) properties in one molecule, but also enable the conversion from p-type to n-type charge transport characteristics.

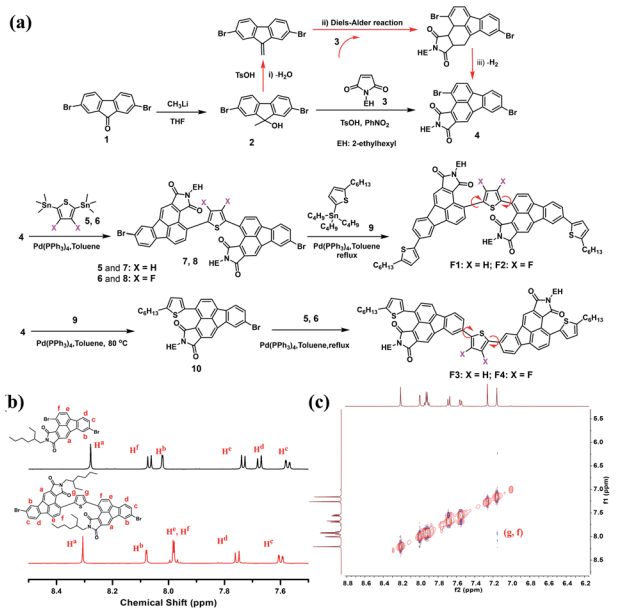

Fig. 2 (a) Synthetic routes for regioregular **F1–F4**; (b) comparison of ^{1}H NMR signals between intermediates **4** and **7**; (c) ^{1}H–^{1}H NOESY spectra of **7**.

Results and discussion

Fig. 2a illustrates the synthetic routes for **F1–F4**. First, 2,7-dibromofluorenone (**1**) reacted with methyllithium to afford compound **2**, which then underwent an optimized one-pot reaction to obtain a new 2,3-fluoranthene imide (**4**) with two bromide atoms substituted at the 4- and 9-sites. As shown, this one-pot reaction involves three consecutive steps; compound **2** first underwent dehydration with a small amount of *p*-toluenesulfonic acid (TsOH) as the catalyst (i), and then the resulting dibenzofulvene product carried out a Diels–Alder reaction with maleimide **3** at 160 °C (ii), followed by dehydrogenation (iii). We further found that the bromine substitutions at the 4- and 9-sites possess different reactivity for the Stille coupling reaction, and the 4-site shows a higher reactivity. By controlling the reaction temperature and the feeding ratio between compounds **4** and **5**, we successfully obtained a new regioregular intermediate (**7**) with an inward imide orientation. The comparison of the ^{1}H NMR spectra of **4** and **7** shows that the proton H^f in **7** has a visible shift to the high field, indicating that the reaction occurs at the 4-site (Fig. 2b). We also performed the ^{1}H–^{1}H NOESY measurements of **7** (Fig. 2c), and the correlation between H^g and H^f reveals that H^f is the proton adjacent to the thiophene group, further confirming the structure. Using the same method, the intermediate **8** was synthesized with two fluorine atoms on the thiophene bridge. Finally, **F1** and **F2** were obtained *via* another Stille coupling reaction with compound **9**. Similarly, **F3** and **F4** with an outward imide orientation were yielded *via* two consecutive coupling reactions; however, the reaction conditions such as temperature need to be carefully optimized. The structure of the critical intermediate **10** was also confirmed by ^{1}H NMR and ^{1}H–^{1}H NOESY spectra as shown in Fig. S1–S2.†

Thermogravimetric analysis was used to study the thermal properties of **F1–F4**, and all exhibit high thermal stability with a 5% weight loss temperature over 410 °C (Fig. S3†). Differential scanning calorimetry (DSC) (Fig. S4†) shows that **F3** exhibits the most intense melting/crystallization peaks at 275.4/238.0 °C, whereas **F1** exhibits the weakest melting/crystallization peaks at 210.5/123.0 °C, indicating a higher crystallinity of **F3** powder (Fig. S5†). Besides, for **F2** and **F4**, the melting/crystallization peaks were shifted to 273.7/244.6 °C and 279.2/247.3 °C, respectively, mainly due to their structural difference induced by the imide direction and fluorination effect.

The absorption spectra of **F1–F4** in dichloromethane (DCM) solutions and as thin films are shown in Fig. 3a and S6,† respectively, with relevant data listed in Table 1. The absorption profiles of **F1** and **F2** have a triple-band shape while **F3** and **F4** have a typical dual-band shape, indicating that the imide orientation has a clear impact on the molecular conjugation. The low-energy absorption band is ascribed to the intramolecular charge transfer (ICT) between the thiophene unit and

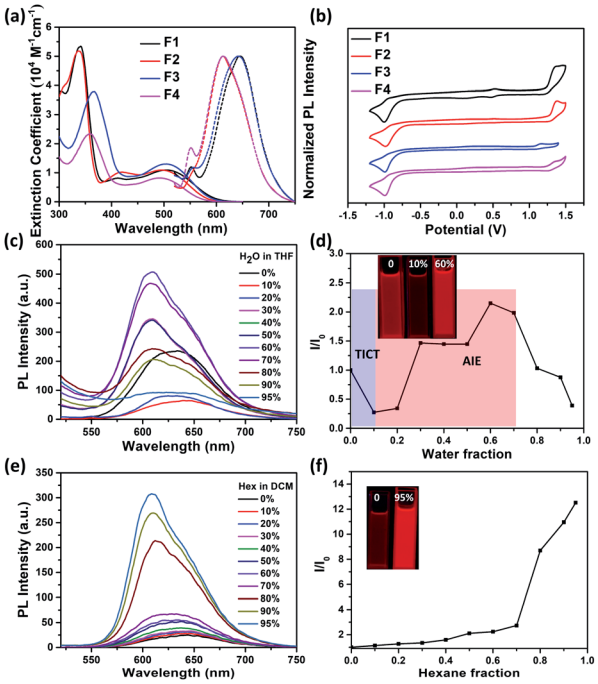

Fig. 3 (a) UV-vis spectra (solid) and normalized emission spectra (dash) and (b) cyclic voltammograms of **F1–F4** in DCM solutions; emission spectra of **F3** in THF/water mixtures (c) and DCM/hexane mixtures (e); plots of (I/I_0) *vs.* f_w in THF/water mixtures (d) and DCM/hexane mixtures (f). Inset: images of **F3** in solution mixtures under 365 nm ultraviolet light.

the imide group, and fluorination leads to a blue-shifted ICT band, ~10 nm. Furthermore, all molecules exhibit a red-shifted ICT absorption band in the solid state, ~30 nm, compared to the solution ones, possibly attributed to the planarization of the conjugated backbone as a result of aggregation. To gain insight into the redox behaviours, cyclic voltammetry (CV) measurements were conducted (Fig. 3b). As listed in Table 1, **F1** and **F2** with an inward imide orientation both exhibit slightly deepened HOMO/LUMO levels compared to those with an outward imide orientation, while fluorination can further slightly decrease the HOMO/LUMO levels due to their enhanced electronegativity.

We further studied their photoluminescence (PL) properties in different organic solvents (Fig. 3a and S7†), with relevant data listed in Table 2. Interestingly, all the PL spectra show an obvious solvatochromic effect; that is, the emission spectra are red-shifted and broadened upon increasing the solvent polarity, accompanied by a significantly decreased PL intensity. This

Table 2 PL data of **F1–F4** in the solution and powder states

	λ_{em} (nm)							
	Hexane	Toluene	THF	DCM	Powder	$\Phi_{PL}{}^a$	$\Phi_{PL}{}^b$	$\Phi_{PL}{}^c$
F1	610	634	643	645	650	2.7%	5.0%	3.8%
F2	577	594	605	613	642	3.0%	7.0%	3.9%
F3	598	615	629	641	640	0.3%	4.3%	5.9%
F4	590	608	613	620	653	2.1%	3.8%	3.8%

[a] Absolute photoluminescence quantum yields tested in DCM solutions. [b] In DCM/hexane mixtures, and the hexane fraction for **F1–F4** is 95%, 70%, 95% and 90%, respectively. [c] In solid powders.

phenomenon can be attributed to the well-known twisted intramolecular charge transfer (TICT) effect, for which the intramolecular rotation can bring the molecule from the locally excited (LE) state to the TICT state in polar solvents, leading to a pronounced charge separation between the D and A units to quench the fluorescence.[47–50]

Encouragingly, the formation of aggregates for **F1–F4** can effectively suppress the negative TICT effect (Fig. 3c–d, S8–S10†). As an example, Fig. 3c–d show the change of the PL intensity of **F3** as a function of water fraction (f_w). When the f_w increases from 0 to 10%, the PL intensity of **F3** is decreased by 50%, accompanied by a red shift, indicating the occurring of a "dark" TICT state. However, when increasing the f_w to 40%, an obvious AIE phenomenon is observed, realizing a ~9-fold intensity enhancement at f_w = 60%. This could be due to the restriction of intramolecular rotation between the D and A units due to the formation of aggregates.[51–54] Note that adding more water further causes a decrease in emission due to sedimentation (Fig. S11†). The emission properties of **F1–F4** in DCM/hexane mixtures were also investigated (Fig. 3e–f, S12–S14†), and upon increasing the apolar hexane fraction, their emission all was increased obviously with a gradual blue-shift, attributed to the synergetic effects from AIE and mitigated TICT. The AIE effect can be further confirmed by dynamic light scattering results (Fig. S15†) as well as enhanced absolute photoluminescence quantum yields (Φ_{PL}s) in DCM/hexane mixtures (Table 2). The above results are indeed encouraging, because (i) most of the imide-based arenes such as PDI and NDI usually suffer from a serious ACQ effect due to their rigid and highly planar structure; (ii) the AIE properties for **F1–F4** are achieved without needing the decoration of any AIE-active building blocks or large steric spacers that usually break the original π-conjugated structure.[29,55–57]

Table 1 Physicochemical and thermal properties and energy levels of **F1–F4**

	λ_{sol} (nm)	λ_{fil} (nm)	$E_g{}^a$ (eV)	HOMO^b (eV)	LUMO^b (eV)	$T_d{}^c$ (°C)	$T_m{}^d$ (°C)
F1	341, 411, 503	344, 530	2.07	−5.51	−3.46	429.6	210.5
F2	337, 420, 493	307, 454, 522	2.12	−5.56	−3.50	417.7	273.7
F3	367, 505	376, 532	2.11	−5.34	−3.44	438.9	275.4
F4	358, 492	369, 519	2.16	−5.50	−3.44	416.2	279.2

[a] Optical energy gaps calculated according to the equation $E_g = 1240/\lambda_{onset}$ eV. [b] Estimated values using the equations $E_{LUMO}/E_{HOMO} = -(4.80 + E_{red}/E_{ox})$ eV. [c] The 5% weight loss temperature. [d] Melting point.

In the solid state, **F1–F4** all show bright red emission (Fig. S16†) with Φ_{PL}s (Table 2) estimated to be 3.8, 3.9, 5.9 and 3.8%, respectively. It is worth noting that both **F2** and **F4** exhibit an obvious red-shifted solid-state emission compared to those in solutions, while no clear change is observed for **F1** and **F3** (Fig. S17† and Table 2), ascribed to the amorphous state of former powders with tight intermolecular interactions confirmed by powder XRD patterns (Fig. S5†).

Theoretical computations were also performed by employing the density functional theory (DFT) method at the B3LYP/6-31G level to understand the effect of the regioregular structure, and the results are shown in Fig. S18.† All molecules show a twisted structure between the thiophene bridge and two fluoranthene imide units. In particular, **F1** and **F2** exhibit much larger dihedral angles than **F3** and **F4**, which can be rationalized by the steric hindrance between the two inward imide units of the former. Possibly due to the larger steric hindrance, the two fluoranthene imides in **F1** are located on the upper and lower sides of the thiophene unit, while they are located on the same sides for the others. In addition, fluorinated **F2** and **F4** both show reduced dihedral angles compared to the corresponding nonfluorinated analog, suggesting enhanced backbone planarity achieved by the non-covalent interactions due to the fluorine substitutions. **F1–F4** also show similar energy level distributions, in which the HOMOs delocalize over the entire conjugated backbone, while the LUMOs mainly localize on the two fluoranthene imide units. Notably, the trend of calculated HOMO/LUMO levels is almost consistent with that obtained by CV measurements.

We further employed grazing-incidence wide angle X-ray scattering (GIWAXS) and atomic force microscope (AFM) measurements to investigate the impact of geometric differences on the crystalline properties and the film morphology. The films were prepared by spin-coating on a SiO_2 dielectric layer and annealing at 180 °C. As shown in Fig. 4a–d, all films show a weak (010) π–π stacking peak along the in-plane direction, being beneficial to charge transport. Both **F1** and **F3** films further show a strong (001) diffraction peak at ~0.35 Å along the out-of-plane direction, assigned to a highly ordered lamella packing. In addition, the **F1** film possesses large crystalline domains with obvious grain boundaries and a large root mean square roughness (RMS) value of 4.7 nm, while **F3** molecules assemble into uniform and compact nanosheets with a small RMS value of 1.7 nm. In principle, the discontinuous grain boundaries observed in **F1** are not favorable for charge transport while the interconnected nanosheets for **F3** are conducive for efficient charge transport.[58,59] As a result, the regioregular configuration exerted by the imide orientation leads to a discrepancy in the molecular packing behavior and film morphology. On the other hand, both **F2** and **F4** films show a ring-like scattering feature with a relatively weak and broadened peak at 0.35 Å along the out-of-plane direction, suggesting a partially ordered lamellar packing but with anisotropy. Moreover, as shown in Fig. 4c–d, they also exhibit a fiber-like feature with large RMS values of 13.7 and 14.3 nm, respectively. Hence, there is a compromise existing between fluorination and regioisomerism for the molecule's crystallinity and aggregation in our case.

We finally examined the charge transport properties of **F1–F4** by fabricating bottom-gate/top-contact (BG/TC) OFETs. The details of device fabrication and characterization are described in the Experimental section in the ESI. Fig. 5 shows the optimized transfer curves of OFET devices based on the films of **F1–F4** annealed at 180 or 200 °C and the detailed performance is summarized in Table 3. The transfer curves based on these films annealed at other temperatures (180 or 250 °C) are presented in Fig. S19.† As seen, all devices show distinguishable FET characteristics, except for **F1** (Fig. 5a). This can be attributed to its twisted molecular structure and unfavorable film morphology as discussed earlier. In contrast, **F3**, the regioisomer of **F1**, delivers a conspicuous p-type characteristic (Fig. 5b) and its corresponding output curves are presented in Fig. S20.† The maximum hole mobility (μ_h) value of a FET device based on the **F3** film reaches 0.026 $cm^2\ V^{-1}\ s^{-1}$, being ~10^4 times greater than the value of **F1**. Note that there are very few reports on fluoranthene-based FETs (Table S1†), and the high μ_h value of **F3** is comparable to that of most solution-processed small molecule semiconductors.[60–62] The critical effect of regioregular structures on the charge transport properties

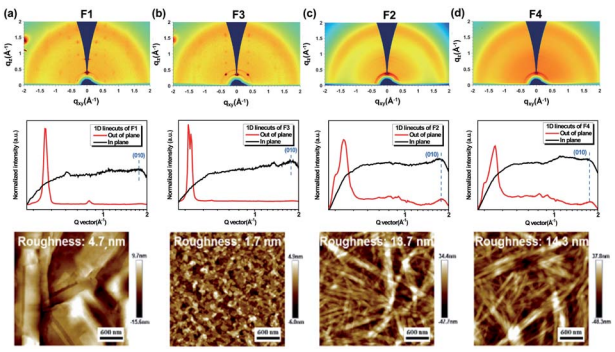

Fig. 4 GIWAXS 2D patterns, 1D scattering profiles, and AFM images of films of (a) **F1**, (b) **F3**, (c) **F2**, and (d) **F4**. Note that all films are annealed at 180 °C.

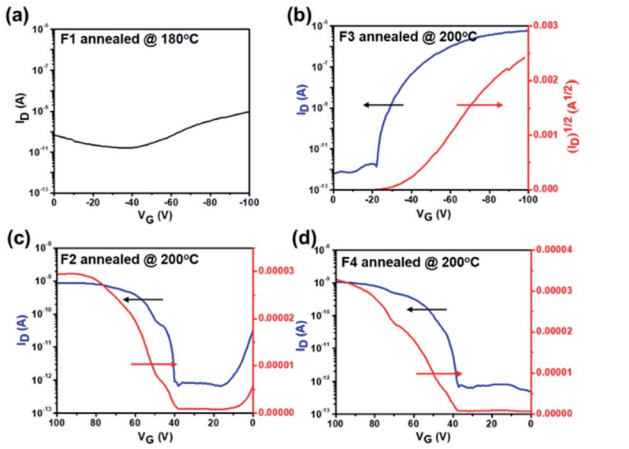

Fig. 5 P-type transfer curves of FET devices based on (a) the **F1** film annealed at 180 °C and (b) the **F3** film annealed at 200 °C. N-type transfer curves of FET devices based on (c) the **F2** film and (d) the **F4** film annealed at 200 °C.

Table 3 Performance of the studied FET devices under different fabrication conditions

	T_{anneal} (°C)	μ ($cm^2\ V^{-1}\ s^{-1}$)	V_T (V)	I_{on}/I_{off}
p-type character		μ_h		
F1	180	3.03×10^{-6}	−46.41	5.8×10^{1}
F3	180	1.88×10^{-3}	−30.88	8.3×10^{6}
F3	200	2.41×10^{-2} $(2.63 \times 10^{-2})^a$	−38.96	1.8×10^{8}
F3	250	2.21×10^{-2}	−50.87	1.7×10^{8}
n-type character		μ_e		
F2	180	2.20×10^{-5}	46.06	1.9×10^{4}
F2	200	5.81×10^{-5} $(1.43 \times 10^{-4})^a$	41.36	2.8×10^{5}
F2	250	1.35×10^{-5}	58.67	5.7×10^{3}
F4	180	6.91×10^{-6}	54.84	9.0×10^{4}
F4	200	2.22×10^{-5} $(3.34 \times 10^{-5})^a$	39.00	5.5×10^{3}
F4	250	1.04×10^{-5}	42.46	1.2×10^{5}

[a] Maximum values in brackets.

closely correlates with their distinct molecular packing patterns and film morphology.[63–66] Here, the outward imide units in **F3** are more favorable for intermolecular packing than the inward ones in **F1**, thereby enabling a much higher μ_h value.

On the other hand, as presented in Fig. 5c–d, both **F2** and **F4** comprising a fluorinated thiophene bridge present n-type characteristics, and their maximum electron mobility (μ_e) values are ~1.43×10^{-4} and ~3.34×10^{-5} $cm^2\ V^{-1}\ s^{-1}$, respectively. Clearly, the fluorination of the bridge thiophene unit changes the polarity of the compounds from p-type to n-type as a result of enhanced electronegativity. We notice that the low μ_e values might be attributed to their inferior crystal orientation. In addition, the LUMO level below −3.6 eV has been considered as the window of trap-free electron transport for n-type semiconductors.[67] Thus, the relatively higher LUMO levels of both **F2** (−3.50 eV) and **F4** (−3.44 eV) could also be responsible for their poor electron transport. Nonetheless, this is the first demonstration of n-type FET devices based on fluoranthene molecules (Table S1†), manifesting the potential of asymmetric 2,3-fluoranthene imide units for new n-type semiconductors. Further device optimization like using Ag electrodes with a more compatible work function to **F2** and **F4** is in progress.

In addition, as presented in Table 3, the annealing temperature of the active layer has a germane correlation with the resultant performance. Due to the high melting points, **F2–F4** films deliver the most optimized FET performance at high annealing temperature (200 °C) as a result of the facilitated molecular packing. Taking **F3** as an example, the FET device based on the as-cast **F3** film shows no distinguishable FET characteristic (Fig. S21†). However, owing to the low melting point, the optimized annealing temperature of the **F1** film is restricted to 180 °C, and annealing the **F1** film at 200 °C results in severe film degradation.

Conclusions

In conclusion, starting from the simple fluorenone, a new type of π-acceptor building block, namely 2,3-fluoranthene imide, is synthesized through a facile one-pot synthetic route. Unlike the fluoranthene imide derivatives reported to date, this new asymmetric building block shows a significant reactivity difference at the 4- and 9-substitution sites, thereby allowing us to successfully synthesize two types of regioisomers (**F1–F4**) with outward and inward imide orientations. We unveil that the distinct molecular geometry for these regioisomers results in different molecular crystallinity in the solid state. Due to the twisted configuration, all molecules exhibit an obvious twisted TICT decay pathway, leading to red-shifted and reduced emission in polar solvents. However, the negative TICT effect can be effectively suppressed by the attractive AIE process, and **F3** shows the brightest red emission at 640 nm in the powder state with the highest Φ_{PL} of 5.9%. The charge transporting abilities of these molecules were systematically studied by fabricating solution-processed FETs. Impressively, **F3** delivers a conspicuous p-type character with a maximum μ_h value of 0.026 $cm^2\ V^{-1}\ s^{-1}$, being ~10^4 times greater than the value of **F1**, owing to its superior crystallinity and film morphology. Moreover, the fluorination on the central thiophene bridge effectively converts the polarity of the molecules from p-type to n-type, resulting in μ_e values of ~1.43×10^{-4} and ~3.34×10^{-5} $cm^2\ V^{-1}\ s^{-1}$ for **F2** and **F4**, respectively. Our results clearly suggest that 2,3-fluoranthene imide is a promising building block for high-performance organic semiconductors with AIE properties.

Data availability

Data associated with this article, including synthetic details, materials characterization and transistor fabrication details are available in the ESI.†

Author contributions

X. Sun and Z. A. Li conceived and designed the study. X. Sun and X. Yu performed the materials synthesis. X. Sun performed the materials characterization. M.-Y. Liao and Y.-S. Wu performed the morphology characterization and the transistor fabrication. C. Zhong performed the DFT calculations. X. Sun, M.-Y. Liao, C.-

C. Chueh and Z. A. Li analyzed the obtained data. X. Sun wrote the original draft. Z. A. Li and C.-C. Chueh reviewed and edited the paper. C.-C. Chueh, Z. Li and Z. A. Li supervised the work. All authors contributed to the finalization of the paper.

Conflicts of interest

There are no conflicts to declare.

Acknowledgements

Z. L. acknowledges the financial support from the Natural Science Foundation of China (No 21975085 and 22175067) and the Innovation and Talent Recruitment Base of New Energy Chemistry and Device (No B21003). X. S. acknowledges the financial support from the China Postdoctoral Science Foundation (2021M691111). C.-C. C acknowledges the financial support from the Ministry of Science and Technology of Taiwan (MOST 110-2634-F-002-043 and 110-2628-E-002-011-) and Top University Project of National Taiwan University (110L7836). The authors from HUST would also like to thank the Analytical and Testing Center at HUST for use of their facilities.

Notes and references

1 D. Li, W.-Y. Lai, Y.-Z. Zhang and W. Huang, *Adv. Mater.*, 2018, **30**, 1704738.
2 C. Cui, D. H. Park and D. J. Ahn, *Adv. Mater.*, 2020, **32**, 2002213.
3 H. Xu, L. Yin, C. Liu, X. Sheng and N. Zhao, *Adv. Mater.*, 2018, **30**, 1800156.
4 A. Facchetti, *Mater. Today*, 2007, **10**, 28–37.
5 L. Duan, J. Qiao, Y. Sun and Y. Qiu, *Adv. Mater.*, 2011, **23**, 1137–1144.
6 T. Lei, J.-Y. Wang and J. Pei, *Acc. Chem. Res.*, 2014, **47**, 1117–1126.
7 Z. Liu, G. Zhang and D. Zhang, *Acc. Chem. Res.*, 2018, **51**, 1422–1432.
8 M. Kim, S. U. Ryu, S. A. Park, K. Choi, T. Kim, D. Chung and T. Park, *Adv. Funct. Mater.*, 2020, **30**, 1904545.
9 J. Zhang, W. Xu, P. Sheng, G. Zhao and D. Zhu, *Acc. Chem. Res.*, 2017, **50**, 1654–1662.
10 X. Liu, Y.-Z. Long, L. Liao, X. Duan and Z. Fan, *ACS Nano*, 2012, **6**, 1888–1900.
11 J. Yang, Z. Zhao, S. Wang, Y. Guo and Y. Liu, *Chem*, 2018, **4**, 2748–2785.
12 Y. Zhao, Y. Guo and Y. Liu, *Adv. Mater.*, 2013, **25**, 5372–5391.
13 C. Dou, X. Long, Z. Ding, Z. Xie, J. Liu and L. Wang, *Angew. Chem., Int. Ed.*, 2016, **55**, 1436–1440.
14 J. E. Anthony, A. Facchetti, M. Heeney, S. R. Marder and X. Zhan, *Adv. Mater.*, 2010, **22**, 3876–3892.
15 B. A. Jones, A. Facchetti, M. R. Wasielewski and T. J. Marks, *J. Am. Chem. Soc.*, 2007, **129**, 15259–15278.
16 M. M. Ling, P. Erk, M. Gomez, M. Koenemann, J. Locklin and Z. Bao, *Adv. Mater.*, 2007, **19**, 1123–1127.
17 X. Zhan, Z. a. Tan, B. Domercq, Z. An, X. Zhang, S. Barlow, Y. Li, D. Zhu, B. Kippelen and S. R. Marder, *J. Am. Chem. Soc.*, 2007, **129**, 7246–7247.
18 H. Yan, Z. Chen, Y. Zheng, C. Newman, J. R. Quinn, F. Dötz, M. Kastler and A. Facchetti, *Nature*, 2009, **457**, 679–686.
19 X. Guo, A. Facchetti and T. J. Marks, *Chem. Rev.*, 2014, **114**, 8943–9021.
20 X. Zhan, A. Facchetti, S. Barlow, T. J. Marks, M. A. Ratner, M. R. Wasielewski and S. R. Marder, *Adv. Mater.*, 2011, **23**, 268–284.
21 Z. A. Li, C. C. Chueh and A. K. Y. Jen, *Prog. Polym. Sci.*, 2019, **99**, 101175.
22 J. Liu, H. Zhang, H. Dong, L. Meng, L. Jiang, L. Jiang, Y. Wang, J. Yu, Y. Sun, W. Hu and A. J. Heeger, *Nat. Commun.*, 2015, **6**, 10032.
23 F. Bu, R. Duan, Y. Xie, Y. Yi, Q. Peng, R. Hu, A. Qin, Z. Zhao and B. Z. Tang, *Angew. Chem., Int. Ed.*, 2015, **54**, 14492–14497.
24 Z. Li and A. Qin, *Natl. Sci. Rev.*, 2014, **1**, 22–24.
25 Y. Huang, J. Xing, Q. Gong, L.-C. Chen, G. Liu, C. Yao, Z. Wang, H.-L. Zhang, Z. Chen and Q. Zhang, *Nat. Commun.*, 2019, **10**, 169.
26 H. Jiang and W. Hu, *Angew. Chem., Int. Ed.*, 2020, **59**, 1408–1428.
27 Z. Qin, H. Gao, H. Dong and W. Hu, *Adv. Mater.*, 2021, **33**, 2007149.
28 D. Liu, Q. Liao, Q. Peng, H. Gao, Q. Sun, J. De, C. Gao, Z. Miao, Z. Qin, J. Yang, H. Fu, Z. Shuai, H. Dong and W. Hu, *Angew. Chem., Int. Ed.*, 2021, **60**, 20274–20279.
29 Z. Zhao, S. M. Gao, X. Y. Zheng, P. F. Zhang, W. T. Wu, R. T. K. Kwok, Y. Xiong, N. L. C. Leung, Y. C. Chen, X. K. Gao, J. W. Y. Lam and B. Z. Tang, *Adv. Funct. Mater.*, 2018, **28**, 1705609.
30 A. Dadvand, A. G. Moiseev, K. Sawabe, W. H. Sun, B. Djukic, I. Chung, T. Takenobu, F. Rosei and D. F. Perepichka, *Angew. Chem., Int. Ed.*, 2012, **51**, 3837–3841.
31 A. J. C. Kuehne and M. C. Gather, *Chem. Rev.*, 2016, **116**, 12823–12864.
32 M. Kyeong, J. Lee, K. Lee and S. Hong, *ACS Appl. Mater. Interfaces*, 2018, **10**, 23254–23262.
33 X. Sun, F. Wu, C. Zhong, L. Zhu and Z. a. Li, *Chem. Sci.*, 2019, **10**, 6899–6907.
34 A. Modelli, L. Mussoni and D. Fabbri, *J. Phys. Chem. A*, 2006, **110**, 6482–6486.
35 L. Ding, C.-Y. Yang, Y.-Q. Zheng, J.-Y. Wang, J. Pei and Z. Su, *Asian J. Org. Chem.*, 2017, **6**, 1231–1234.
36 Y. Zhou, Y. Z. Dai, Y. Q. Zheng, X. Y. Wang, J. Y. Wang and J. Pei, *Chem. Commun.*, 2013, **49**, 5802–5804.
37 S. Chatterjee, Y. Ie, T. Seo, T. Moriyama, G.-J. A. H. Wetzelaer, P. W. M. Blom and Y. Aso, *NPG Asia Mater.*, 2018, **10**, 1016–1028.
38 Y. Q. Zheng, Y. Z. Dai, Y. Zhou, J. Y. Wang and J. Pei, *Chem. Commun.*, 2014, **50**, 1591–1594.
39 Y. Zhou, L. Ding, K. Shi, Y.-Z. Dai, N. Ai, J. Wang and J. Pei, *Adv. Mater.*, 2012, **24**, 957–961.
40 H. Ishikawa, K. Katayama, J.-i. Nishida, C. Kitamura and T. Kawase, *Tetrahedron Lett.*, 2018, **59**, 3782–3786.

41 L. Ding, C. Yang, Z. Su and J. Pei, *Sci. China: Chem.*, 2015, **58**, 364–369.
42 L. Ding, H. Z. Ying, Y. Zhou, T. Lei and J. Pei, *Org. Lett.*, 2010, **12**, 5522–5525.
43 Q. Yan, Y. Zhou, B.-B. Ni, Y. Ma, J. Wang, J. Pei and Y. Cao, *J. Org. Chem.*, 2008, **73**, 5328–5339.
44 Y. Kunugi, T. Kosuge and K. Okamoto, *Electrochemistry*, 2008, **76**, 865–867.
45 X. Sun, Q. Xue, Z. Zhu, Q. Xiao, K. Jiang, H.-L. Yip, H. Yan and Z. a. Li, *Chem. Sci.*, 2018, **9**, 2698–2704.
46 X. Yu, Z. Li, X. Sun, C. Zhong, Z. Zhu, Z. a. Li and A. K. Y. Jen, *Nano Energy*, 2021, **82**, 105701.
47 J. Mei, Y. Hong, J. W. Y. Lam, A. Qin, Y. Tang and B. Z. Tang, *Adv. Mater.*, 2014, **26**, 5429–5479.
48 J. Katuri, X. Ma, M. M. Stanton and S. Sánchez, *Acc. Chem. Res.*, 2017, **50**, 2–11.
49 R. Hu, E. Lager, A. Aguilar-Aguilar, J. Liu, J. W. Y. Lam, H. H. Y. Sung, I. D. Williams, Y. Zhong, K. S. Wong, E. Peña-Cabrera and B. Z. Tang, *J. Phys. Chem. C*, 2009, **113**, 15845–15853.
50 Z. R. Grabowski, K. Rotkiewicz and W. Rettig, *Chem. Rev.*, 2003, **103**, 3899–4032.
51 J. Yang, Z. Chi, W. Zhu, B. Z. Tang and Z. Li, *Sci. China: Chem.*, 2019, **62**, 1090–1098.
52 Z. Zhao, H. Zhang, J. W. Y. Lam and B. Z. Tang, *Angew. Chem., Int. Ed.*, 2020, **59**, 9888–9907.
53 Y. Li, Z. Cai, S. Liu, H. Zhang, S. T. H. Wong, J. W. Y. Lam, R. T. K. Kwok, J. Qian and B. Z. Tang, *Nat. Commun.*, 2020, **11**, 1255.
54 K. Katayama, I. Kawajiri, Y. Okano, J. I. Nishida and T. Kawase, *Chempluschem*, 2019, **84**, 722–729.
55 D. Guo, L. Li, X. Q. Zhu, M. Heeney, J. Li, L. C. Dong, Q. S. Yu, Z. H. Gan, X. G. Gu and L. X. Tan, *Sci. China: Chem.*, 2020, **63**, 1198–1207.
56 L. Zong, Y. Xie, C. Wang, J. R. Li, Q. Li and Z. Li, *Chem. Commun.*, 2016, **52**, 11496–11499.
57 Q. Li and Z. Li, *Acc. Chem. Res.*, 2020, **53**, 962–973.
58 Y. Zhang, C. Kim, J. Lin and T. Q. Nguyen, *Adv. Funct. Mater.*, 2012, **22**, 97–105.
59 G. Zhang, Y. Zhao, B. Kang, S. Park, J. Ruan, H. Lu, L. Qiu, Y. Ding and K. Cho, *Chem. Mater.*, 2019, **31**, 2027–2035.
60 A. F. Paterson, S. Singh, K. J. Fallon, T. Hodsden, Y. Han, B. C. Schroeder, H. Bronstein, M. Heeney, I. McCulloch and T. D. Anthopoulos, *Adv. Mater.*, 2018, **30**, 1801079.
61 M. Chen, L. Yan, Y. Zhao, I. Murtaza, H. Meng and W. Huang, *J. Mater. Chem. C*, 2018, **6**, 7416–7444.
62 K. Takimiya, M. Nakano, H. Sugino and I. Osaka, *Synth. Met.*, 2016, **217**, 68–78.
63 L. H. Jimison, M. F. Toney, I. McCulloch, M. Heeney and A. Salleo, *Adv. Mater.*, 2009, **21**, 1568–1572.
64 T. Bjørnholm, D. R. Greve, N. Reitzel, T. Hassenkam, K. Kjaer, P. B. Howes, N. B. Larsen, J. Bøgelund, M. Jayaraman, P. C. Ewbank and R. D. McCullough, *J. Am. Chem. Soc.*, 1998, **120**, 7643–7644.
65 D. H. Kim, Y. D. Park, Y. Jang, H. Yang, Y. H. Kim, J. I. Han, D. G. Moon, S. Park, T. Chang, C. Chang, M. Joo, C. Y. Ryu and K. Cho, *Adv. Funct. Mater.*, 2005, **15**, 77–82.
66 Y. Wang, H. Tatsumi, R. Otsuka, T. Mori and T. Michinobu, *J. Mater. Chem. C*, 2018, **6**, 5865–5876.
67 N. B. Kotadiya, A. Mondal, P. W. M. Blom, D. Andrienko and G.-J. A. H. Wetzelaer, *Nat. Mater.*, 2019, **18**, 1182–1186.